CAV2009 – Paper No. 52

Numerical Simulation of Unsteady Three-Dimensional Sheet Cavitation

Arjen Koop
MARIN
Wageningen, the Netherlands

Harry Hoeijmakers
University of Twente
Enschede, the Netherlands

ABSTRACT

The shedding of a sheet cavity is governed by the direction and momentum of re-entrant and side-entrant jets and their impingement on the free surface of the cavity. Therefore, for an accurate prediction of the shedding of the sheet cavity it is important to predict the re-entrant and side-entrant jets accurately. It appears that these jets are inertia driven suggesting that a numerical method based on the Euler equations is able to capture the phenomena associated with unsteady sheet cavitation.

Due to the dynamics of sheet cavitation, strong pressure pulses are generated, originating from the collapse of shed vapor structures. To be able to predict the dynamics of the pressure waves the fluid is considered as a compressible medium by adopting appropriate equations of state for the liquid phase, the two-phase mixture and the vapor phase of the fluid.

In this paper a computational method for solving the compressible unsteady Euler equations on unstructured grids is employed to predict the structure and dynamics of three-dimensional unsteady sheet cavitation occurring on stationary hydrofoils, placed in a steady uniform flow. In the two-phase flow region an equilibrium cavitation model is employed, which assumes local thermodynamic and mechanical equilibrium. In this model the phase transition does not depend on empirical constants to be specified.

The three-dimensional unsteady cavitating flow about a three-dimensional hydrofoil (Twist11) is calculated. It is shown that the formation of the re-entrant flow and a cavitating horse-shoe vortex are captured by the present numerical method. The calculated results agree reasonably well with experimental observations. Furthermore, it is demonstrated that the collapse of the shed vapor structures and the resulting high pressure pulses are captured in the numerical simulations.

INTRODUCTION

Cavitation is the evaporation of a liquid in a flow when the pressure drops below the saturation pressure of that liquid. The importance of understanding cavitating flows is related to their occurrence in various technical applications, such as pumps, turbines, ship propellers and fuel injection systems, as well as in medical sciences such as lithotripsy treatment and the flow through artificial heart valves. Cavitation does not occur in water only, but in any kind of liquid such as liquid hydrogen and oxygen in rocket pumps or the lubricant in a bearing. The appearance and disappearance of regions with vapor is a major cause of noise, vibration, erosion of surface material and efficacy loss in hydraulic machinery. In many technical applications high efficiency is required, which results in cavitation being hardly avoidable within the range of operating conditions. When cavitation occurs it needs to be controlled. Therefore, one needs detailed insight in the mechanisms that govern the cavitation phenomena.

The present paper concerns the dynamics and structure of sheet cavitation, which occurs on lifting objects such as hydrofoils, blades of pumps and propellers. There are a number of closely related important aspects to sheet cavitation:

• *Shape and volume of the cavity*. The topology of a sheet cavity is strongly related to the load distribution of the lifting object and thus to the pressure distribution on the surface of the object. Variations in volume cause pressure fluctuations in the liquid that might lead to strong vibrations of nearby structures.

• *Re-entrant flow at the closure region of the sheet cavity*. The re-entrant and side-entrant flow dictate the behavior of the shedding of the sheet cavity. The shape of the closure region of the sheet cavity dictates the direction of the re-entrant and side-entrant jets.

• *Shedding and collapse of vapor structures*. The break-up of a sheet cavity causes a vortical flow of bubbly vapor clouds that is convected to regions with higher pressure. Here, these clouds collapse resulting in strong pressure pulses leading to unsteady loads on nearby objects as well as noise production and possible erosion of surface material.

Since the 1990s numerical methods based on the Euler or Navier-Stokes equations have been developed to simulate cavitating flows. Although the development of these methods has been advancing quickly in recent years, they are still considered to be in a developing stage. The main problem in the numerical simulation of multi-dimensional unsteady cavitating flow is the simultaneous treatment of two very different flow regions: (nearly) incompressible flow of pure liquid in most of the flow domain and low-velocity highly

compressible flow of (pure) vapor in relatively small parts of the flow domain. In addition, the two flow regimes can often not be distinguished that clearly, for example in the transition region between vapor and liquid, i.e. the mixture region of liquid and vapor.

Furthermore, unsteady three-dimensional cavitating flow calculations require an appropriate high-resolution mesh in the cavitating flow region, which demands substantial computer resources both in terms of memory and speed.

In the present paper a numerical method for solving the Euler equations for 3D unsteady cavitating flow is described. The accurate prediction of the direction and momentum of the re-entrant and side-entrant jets and their impingement on the cavity surface form the basis of an accurate prediction of the shedding of the cavity sheet. The re-entrant jets are thought to be inertia driven, so it is expected that a mathematical model based on the Euler equations is able to capture the structure of sheet cavitation.

DEFINITIONS DIMENSIONLESS PARAMETERS

The dimensionless cavitation number σ is defined as:

$$\sigma \equiv \frac{p_\infty - p_{sat}(T)}{\frac{1}{2}\rho_\infty U_\infty^2},\qquad(1)$$

where p_∞ [Pa], ρ_∞ [kgm^{-3}] and U_∞ [ms^{-1}] are the free-stream pressure, density and velocity, respectively and where $p_{sat}(T)$ [Pa] is the saturation pressure of water at temperature T [K].

The dimensionless pressure coefficient C_p is defined as

$$C_p \equiv \frac{p - p_\infty}{\frac{1}{2}\rho_\infty U_\infty^2},\qquad(2)$$

with p the local pressure in the flow field. Neglecting skin friction, the drag and lift can be obtained from

$$\vec{F} = \int_S p\vec{n}dS,\qquad(3)$$

with S the surface of the object, p the pressure on the surface of the object and $\vec{n}$ the unit normal pointing into the object, i.e. out of the computational domain. We choose the coordinates such that the lift force L is equal to F_z and the drag force D is equal to F_x. The dimensionless C_L and C_D coefficients are defined as

$$C_L \equiv \frac{L}{\frac{1}{2}\rho_\infty U_\infty^2 S},\ C_D \equiv \frac{D}{\frac{1}{2}\rho_\infty U_\infty^2 S},\qquad(4)$$

with S the projected surface area of the object.

The void fraction $\alpha \equiv V_v/V$ of the vapor within a volume V [m^3] of a fluid follows from the fluid density ρ:

$$\rho = \alpha\rho_{v,sat}(T) + (1-\alpha)\rho_{l,sat}(T),\qquad(5)$$

$$\stackrel{Eq(5)}{\Rightarrow}\qquad \alpha = \frac{\rho - \rho_{l,sat}(T)}{\rho_{v,sat}(T) - \rho_{l,sat}(T)},\qquad(6)$$

where V_v [m^3] is the volume of vapor within the volume V of the fluid and where $\rho_{v,sat}(T)$ [kgm^{-3}] and $\rho_{l,sat}(T)$ [kgm^{-3}] are the saturated vapor and liquid density at temperature T, respectively.

The dimensionless total vapor volume V_{vap} is defined as

$$V_{vap} \equiv \frac{1}{c^3}\sum_{i=1}^N \alpha_i V_i,\qquad(7)$$

with c [m] the chord length of the hydrofoil and N the total number of control volumes in the computational domain.

The Strouhal number St_c based on the chord length c is defined as

$$St_c \equiv \frac{fc}{U_\infty},\qquad(8)$$

with f [Hz] the frequency of the shedding phenomenon.

MATHEMATICAL FORMULATION

Following Saurel *et al.* [15] and Schmidt *et al.* [16] the equilibrium cavitation model is adopted. This physical model is based on the assumption that the two-phase flow regime can be described as a homogeneous mixture of vapor and liquid that remains in thermodynamic and mechanical equilibrium. This implies that in the mixture locally the vapor and liquid have equal temperature, pressure and velocity. Under these assumptions, the flow of the mixture can be described by the homogeneous mixture equations together with an appropriate equation of state that covers all fluid states possible: the compressible pure liquid state, the compressible two-phase mixture state and the compressible pure vapor state. The equations of state must be such that the hyperbolic nature of the system of governing equations is preserved, which is necessary to represent the propagation of pressure waves in the fluid.

The governing equations are the Euler equations in conservation form for the mixture variables written here for Cartesian coordinates as:

$$\frac{\partial \mathbf{U}}{\partial t} + \frac{\partial \mathbf{F}_x(\mathbf{U})}{\partial x} + \frac{\partial \mathbf{F}_y(\mathbf{U})}{\partial y} + \frac{\partial \mathbf{F}_z(\mathbf{U})}{\partial z} = \mathbf{0},\qquad(9)$$

or in integral conservation form as:

$$\frac{\partial}{\partial t}\iiint_\Omega \mathbf{U}d\Omega + \iint_{A=\partial\Omega} \vec{\mathbf{F}}(\mathbf{U})\cdot\vec{n}dA = \mathbf{0}.\qquad(10)$$

Here, $\mathbf{U} = [\rho, \rho u, \rho v, \rho w, \rho E]^T$ is the vector of conserved variables and $\vec{\mathbf{F}}(\mathbf{U}) = [\mathbf{F}_x(\mathbf{U}), \mathbf{F}_y(\mathbf{U}), \mathbf{F}_z(\mathbf{U})]^T$ the flux vector given as

$$\vec{\mathbf{F}}(\mathbf{U}) = \begin{bmatrix} \rho u & \rho v & \rho w \\ \rho u^2 + p & \rho uv & \rho uw \\ \rho uv & \rho v^2 + p & \rho vw \\ \rho uw & \rho vw & \rho w^2 + p \\ \rho Hu & \rho Hv & \rho Hw \end{bmatrix},\qquad(11)$$

where the total specific enthalpy H [Jkg^{-1}] is equal to

$$H = E + \frac{p}{\rho} = h + \frac{1}{2}\vec{u}\cdot\vec{u},\qquad(12)$$

with the total specific energy E [Jkg^{-1}] defined by

$$E = e + \frac{1}{2}\vec{u}\cdot\vec{u},\qquad(13)$$

and with e [Jkg^{-1}] the internal specific energy.

The normal component of the inviscid flux vector $\vec{F}(U) \cdot \vec{n}$ in equation (10) can now be found as

$$\vec{F}(U) \cdot \vec{n} = F_x(U)n_x + F_y(U)n_y + F_z(U)n_z, \quad (14)$$

which yields

$$\vec{F}(U) \cdot \vec{n} = \begin{bmatrix} \rho\hat{u} \\ \rho\hat{u}u + pn_x \\ \rho\hat{u}v + pn_y \\ \rho\hat{u}w + pn_z \\ \rho\hat{u}H \end{bmatrix}, \quad (15)$$

where $\hat{u}$ is the contravariant velocity component normal to the surface A defined by

$$\hat{u} = \vec{u} \cdot \vec{n} = un_x + vn_y + wn_z. \quad (16)$$

For closure of the system of equations it is necessary to adopt equations of state $\rho = \rho(p,T)$ and $h = h(p,T)$ that describe each of the three possible states: the liquid state, the vapor state and the mixture state. In the following the liquid phase is denoted by subscript l, the vapor phase by subscript v and saturation conditions by subscript sat. The speed of sound c [ms^{-1}] within each state is obtained from [12]

$$c^2 = \frac{\rho\left(\frac{\partial h}{\partial T}\right)_p}{\rho\left(\frac{\partial \rho}{\partial p}\right)_T\left(\frac{\partial h}{\partial T}\right)_p + \left(\frac{\partial \rho}{\partial T}\right)_p\left\{1 - \rho\left(\frac{\partial h}{\partial p}\right)_T\right\}}. \quad (17)$$

LIQUID PHASE

Following Saurel *et al.* [15] a modification of Tait's equation of state is used to describe the pressure in the liquid state as a function of the density and temperature:

$$p_l(\rho_l, T_l) = K_0\left[\left(\frac{\rho_l}{\rho_{l,sat}(T_l)}\right)^N - 1\right] + p_{sat}(T_l), \quad (18)$$

where for water $K_0 = 3.3 \cdot 10^8$ Pa and $N = 7.15$ are taken to be constant. A caloric equation of state that is a good approximation, see [12], is given by

$$e_l(\rho_l, T_l) = e_l(T_l) = C_{vl}(T_l - T_0) + e_{l0}, \quad (19)$$

where C_{vl} is the specific heat at constant volume, T_0 is a reference temperature and e_{l0} is the internal energy at this reference temperature. For water these constants have the values $C_{vl} = 4180$ Jkg^{-1}K^{-1}, $T_0 = 273.15$ K and $e_{l0} = 617.0$ Jkg^{-1}, respectively.

VAPOR PHASE

For the vapor phase the equation of state for a calorically perfect gas is used:

$$p_v(\rho_v, e_v) = (\gamma - 1)\rho_v e_v(\rho_v, T_v), \quad (20)$$

with γ the ratio of the specific heats equal to $\gamma = 1.327$ for water vapor. The corresponding caloric equation of state is

$$e_v(\rho_v, T_v) = e_v(T_v) = C_{vv}(T_v - T_0) + L_v(T_0) + e_{l0}, \quad (21)$$

where L_v represents the latent heat of vaporization, T_0 is a reference temperature and C_{vv} the specific heat at constant volume with values equal to $L_v(T_0) = 2.3753 \cdot 10^6$ Jkg^{-1}, $T_0 = 273.15$ K and $C_{vv} = 1410.8$ Jkg^{-1}K^{-1}, respectively.

MIXTURE PHASE

In the mixture the two phases are assumed to be in thermal and mechanical equilibrium. Furthermore, the pressure in the mixture phase is taken to be equal to the saturation pressure:

$$p_l = p_v = p_{sat}(T). \quad (22)$$

The mixture density ρ and mixture internal energy e are defined by

$$\rho = \alpha\rho_{v,sat}(T) + (1-\alpha)\rho_{l,sat}(T), \quad (23)$$

$$\rho e = \alpha\rho_{v,sat}(T)e_v(T) + (1-\alpha)\rho_{l,sat}(T)e_l(T), \quad (24)$$

where the void fraction α of the vapor is obtained from Equation (6).

The saturation values, as a function of temperature, of the pressure $p_{sat}(T)$, the liquid density $\rho_{l,sat}(T)$ and vapor density $\rho_{v,sat}(T)$ are given by the following analytical expressions [17], valid for the range $T = [T_r, T_c]$ with T_r the temperature at the triple point and T_c the temperature at the critical point:

$$\ln\left(\frac{p_{sat}(T)}{p_c}\right) = \frac{T_c}{T}\sum_{i=1}^{7}a_i\theta^{\hat{a}_i}, \quad (25)$$

$$\frac{\rho_{l,sat}(T)}{\rho_c} = \sum_{i=1}^{7}b_i\theta^{\hat{b}_i}, \quad (26)$$

$$\ln\left(\frac{\rho_{v,sat}(T)}{\rho_c}\right) = \sum_{i=1}^{7}c_i\theta^{\hat{c}_i}, \quad (27)$$

where $\theta = 1 - T/T_c$, with p_c and ρ_c the pressure and density at the critical point and where the coefficients $a_i, \hat{a}_i, b_i, \hat{b}_i, c_i$ and $\hat{c}_i$ are included in Table 1. Table 2 gives an overview of the values of the parameters used in the equations of state for liquid and vapor.

In Figure 1 the p-v diagram for water, with the isotherm at reference temperature $T_\infty = 298$ K, is presented. The employed equations of state, i.e. modified Tait equation, the mixture state and the perfect gas equation of state are compared with IAPWS experimental data, see [9].

Table 1: *Parameters for the saturation relations [17].* $T_c = 647.16$ K, $p_c = 221.2 \cdot 10^5$ Pa, $\rho_c = 322.0$ kgm^{-3}, $T_r = 273.15$ K.

i	a_i	$\hat{a}_i$	b_i	$\hat{b}_i$	c_i	$\hat{c}_i$
1	0	0	1	0	0	0
2	-7.85823	1	1.99206	1/3	-2.02957	2/6
3	1.83991	3/2	1.10123	2/3	-2.68781	4/6
4	-11.7811	3	-0.512506	5/3	-5.38107	8/6
5	22.6705	7/2	-1.75263	16/3	-17.3151	18/6
6	-15.9393	4	-45.4485	43/3	-44.6384	37/6
7	1.77516	15/2	-675615	110/3	-64.3486	71/6

Table 2: *Parameters for liquid and vapor phase of water.*

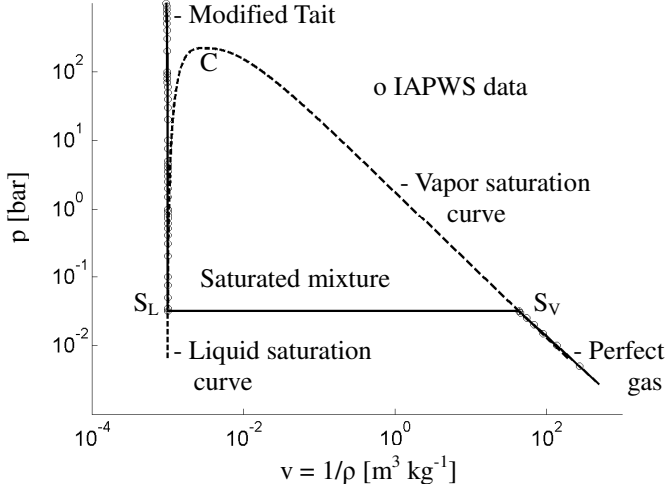| Liquid		Vapor	
Parameter	Value	Parameter	value
N	7.15	γ	1.327
K_0	$3.3 \cdot 10^8$ Pa	C_{vv}	1410.8 Jkg^{-1}K^{-1}
C_{vl}	4180 Jkg^{-1}K^{-1}	T_0	273.15 K
T_0	273.15 K	Lv(T0)	$2.753 \cdot 10^6$Jkg^{-1}
e_{l0}	617.0 Jkg^{-1}	e_{l0}	617.0 Jkg^{-1}

Figure 1: *p-v diagram for water with isotherm at reference temperature T_∞= 298 K. Presented are IAPWS experimental data [17] (open circles), saturation curves for liquid and vapor (dashed lines), saturation points S_L and S_V for liquid and vapor, respectively, modified Tait equation of state for the liquid, mixture state and perfect gas equation of state (solid lines). C is the critical point.*

NUMERICAL METHOD

The homogeneous mixture equations presented in Equation (10) are solved employing an unstructured grid, edge-based, finite-volume method. Dividing the physical domain in control volumes V_i with boundary ∂V_i, Equation (10) can be considered for each control volume:

$$\frac{\partial}{\partial t}\iiint_{V_i} \mathbf{U}d\Omega + \iint_{S=\partial V_i} \vec{\mathbf{F}}(\mathbf{U})\cdot\vec{\mathbf{n}}dS = \mathbf{0}. \qquad (28)$$

Defining the control volume averages $\bar{\mathbf{U}}_i$ as

$$\bar{\mathbf{U}}_i = \frac{1}{|V_i|}\iiint_{V_i} \mathbf{U}d\Omega, \qquad (29)$$

with $|V_i|$ the volume of control volume V_i. Taking into account that $S = \sum_{j=1}^{N_{f_i}}|S_{ij}|$, with N_{f_i} the total number of faces S_{ij} of control volume V_i, Equation (28) can be rewritten as

$$\frac{\partial\bar{\mathbf{U}}_i}{\partial t}+\frac{1}{|V_i|}\sum_{j=1}^{N_{f_i}}\iint_{S_{ij}}\vec{\mathbf{F}}(\mathbf{U})\cdot\vec{\mathbf{n}}_{ij}dS = \mathbf{0}. \qquad (30)$$

The flux $\vec{\mathbf{F}}(\mathbf{U})\cdot\vec{\mathbf{n}}$ can be evaluated by exploiting the rotational invariance property of the Euler equations [12], which states that

$$\mathbf{F}_x(\mathbf{U})n_x + \mathbf{F}_y(\mathbf{U})n_y + \mathbf{F}_z(\mathbf{U})n_z = \mathbf{T}^{-1}\mathbf{F}_x(\mathbf{TU}), \qquad (31)$$

with T the rotation matrix and T^{-1} its inverse given in terms of the elements of the unit normal vector $\vec{\mathbf{n}} = [n_x, n_y, n_z]^T$ and unit tangential vectors $\vec{\mathbf{t}}_1 = [t_{1,x}, t_{1,y}, t_{1,z}]^T$, $\vec{\mathbf{t}}_2 = [t_{2,x}, t_{2,y}, t_{2,z}]^T$ by

$$\mathbf{T} = \begin{bmatrix} 1 & 0 & 0 & 0 & 0 \\ 0 & n_x & n_y & n_z & 0 \\ 0 & t_{1,x} & t_{1,y} & t_{1,z} & 0 \\ 0 & t_{2,x} & t_{2,y} & t_{2,z} & 0 \\ 0 & 0 & 0 & 0 & 1 \end{bmatrix}, \mathbf{T}^{-1} = \begin{bmatrix} 1 & 0 & 0 & 0 & 0 \\ 0 & n_x & t_{1,x} & t_{2,x} & 0 \\ 0 & n_y & t_{1,y} & t_{2,y} & 0 \\ 0 & n_z & t_{1,z} & t_{2,z} & 0 \\ 0 & 0 & 0 & 0 & 1 \end{bmatrix}. \qquad (32)$$

Note that the unit vectors $\vec{\mathbf{n}}, \vec{\mathbf{t}}_1, \vec{\mathbf{t}}_2$ form an orthogonal system. Equation (30) can now be rewritten as:

$$\frac{\partial\bar{\mathbf{U}}_i}{\partial t}+\frac{1}{|V_i|}\sum_{j=1}^{N_{f_i}}\iint_{S_{ij}}\mathbf{T}^{-1}\mathbf{F}_x(\mathbf{TU})dS = \mathbf{0}. \qquad (33)$$

The inter-cell flux $\mathbf{F}_x(\mathbf{TU})$ over face S_{ij} can be approximated by the numerical flux $\mathbf{H}(\mathbf{TU}_L, \mathbf{TU}_R)$, where the extrapolated face values U_L and U_R depend on the control volume averages $\bar{\mathbf{U}}_i$ and $\bar{\mathbf{U}}_j$ on either side of interface S_{ij}. Before proceeding the following notation is introduced for the numerical flux:

$$\mathbf{T}^{-1}\mathbf{F}_x(\mathbf{TU}) \approx \mathbf{T}^{-1}\mathbf{H}(\mathbf{TU}_L, \mathbf{TU}_R) \equiv \mathbf{H}(\mathbf{U}_L, \mathbf{U}_R, \vec{\mathbf{n}}_{ij}), \qquad (34)$$

where the unit normal vector $\vec{\mathbf{n}}_{ij}$ of face S_{ij} defines the rotation matrices T and T^{-1}.

Applying equation (34) to (33) and assuming that the numerical flux H is constant over face S_{ij}, the semi-discretized form of the finite-volume formulation reads:

$$\frac{\partial\bar{\mathbf{U}}_i}{\partial t}+\frac{1}{|V_i|}\sum_{j=1}^{N_{f_i}}\mathbf{H}(\mathbf{U}_L, \mathbf{U}_R, \vec{\mathbf{n}}_{ij})|S_{ij}| = \mathbf{0}. \qquad (35)$$

Note that when the face S_{ij} belongs to the boundary of the computational domain, then it is necessary to determine U_L or U_R from boundary conditions. Also, when $\mathbf{U}_L = \bar{\mathbf{U}}_i$ and $\mathbf{U}_R = \bar{\mathbf{U}}_j$, then the finite-volume scheme is first-order accurate when an approximate Riemann solver is used. In this study the extension to higher order is achieved by considering piece-wise linear data reconstructions in each control volume based on the MUSCL approach of van Leer [13]. The extrapolated face values U_L and U_R are then obtained through

$$\mathbf{U}_L = \bar{\mathbf{U}}_i + \mathbf{\Psi}_i\left[(\nabla\mathbf{U})_{cg,i}\cdot(\vec{\mathbf{x}}_{ij}-\vec{\mathbf{x}}_{cg,i})\right], \qquad (36)$$

$$\mathbf{U}_R = \bar{\mathbf{U}}_j + \mathbf{\Psi}_j\left[(\nabla\mathbf{U})_{cg,j}\cdot(\vec{\mathbf{x}}_{ij}-\vec{\mathbf{x}}_{cg,j})\right], \qquad (37)$$

where $(\nabla\mathbf{U})_{cg,i}$ is the gradient of the variables U at the centroid of control volume V_i and where $\vec{\mathbf{x}}_{ij}$ and $\vec{\mathbf{x}}_{cg,i}$ are the location

of the center of the face S_{ij} and the center of gravity of control volume V_i, respectively. Furthermore, the limiter function $\Psi \in [0,1]$ is applied to avoid spurious oscillations at the cell interfaces. Here, the limiter function of Venkatakrishnan [23] is used.

Defining the residual $\mathfrak{R}_i^n$ at time level t^n for control volume V_i as:

$$\mathfrak{R}_i^n = \frac{1}{|V_i|} \sum_{j=1}^{N_{fi}} \mathbf{H}\left(\mathbf{U}_L^n, \mathbf{U}_R^n, \vec{\mathbf{n}}_{ij}\right) \left|S_{ij}\right|, \qquad (38)$$

then equation (35) can be written as

$$\frac{\partial \bar{\mathbf{U}}_i}{\partial t} + \mathfrak{R}_i^n = \mathbf{0}. \qquad (39)$$

To advance the solution from time level t^n to time level t^{n+1} a standard low-storage four-stage Runge-Kutta time-integration method is employed, which is defined as follows:

$$\mathbf{U}_i^{(0)} = \bar{\mathbf{U}}_i^n, \qquad (40)$$

$$\mathbf{U}_i^{(k)} = \mathbf{U}_i^{(0)} - \alpha_k \Delta t \mathfrak{R}_i^{k-1}, \text{ for k=1,...,4} \qquad (41)$$

$$\bar{\mathbf{U}}_i^{n+1} = \mathbf{U}_i^{(4)}, \qquad (42)$$

with the coefficients α_k equal to [0.1084,0.2602,0.5052,1.0], resulting in second-order accuracy in time, see Blazek [1]. For unsteady flow calculations the time step Δt is a global time step defined as the minimum of the local time steps of all control volumes:

$$\Delta t = \min_i \Delta t_i, \qquad (43)$$

where the local time step is defined by

$$\Delta t_i = C \frac{\ell_i}{\max\left(|\vec{\mathbf{u}}_i| + c_i, |\vec{\mathbf{u}}_i|\right)}, \qquad (44)$$

with ℓ_i a characteristic length of control volume V_i defined as the diameter of the smallest inscribed sphere of control volume V_i and where $\vec{\mathbf{u}}_i$ and c_i are the local velocity vector and speed of sound in control volume V_i, respectively. The constant CFL number C is set to 0.8.

In the present research a number of classical flux schemes has been investigated for the numerical flux $\mathbf{H}(\mathbf{U}_L, \mathbf{U}_R, \vec{\mathbf{n}}_{ij})$. At first, the Jameson-Schmidt-Turkel (JST) scheme [6] with the preconditioning method of Weiss & Smith [25] has been investigated. However, it was found that for cavitating flows the JST scheme introduced small oscillations at sharp gradients of the density in the flow. These oscillations were disastrous for the stability of the numerical method.

In the search for a more robust, stable and accurate scheme other flux schemes have been investigated, such as the HLLC scheme, see Harten, Lax and van Leer [6], Toro *et al.* [22] and Batten *et al.* [1] , and the AUSM scheme and its extensions, see Liou [14].

The stability and accuracy of the scheme is not only influenced by sharp gradients of the density in the flow. The so-called low-Mach number problem is also very important. A popular technique to solve this problem has been to introduce suitable preconditioners. In more recent years, adaptation of the flux schemes by scaling or modifying the numerical dissipation in regions with low-Mach number flows have been found to be successful, e.g. Guillard & Viozat [5], Liou [14] and Schmidt *et al.* [16], [18]. In this research the flux scheme of Schnerr *et al.* [18] is employed, which overcomes the inaccurate calculations of the pressure field for (low-Mach number) liquid flows.

BOUNDARY CONDITIONS

The treatment of the boundary conditions is based on the conventional ghost-cells approach, which implies that the numerical flux over a boundary interface is determined with the same numerical flux as used for internal cells. When the face S_{ij} considered is located on the boundary of the computational domain the right state U_R for the numerical flux $\mathbf{H}(\mathbf{U}_L, \mathbf{U}_R, \vec{\mathbf{n}}_{ij})$ at the cell-interface can be reconstructed from the state U_g in a virtual control volume or "ghost" cell. The state U_g in the ghost cell is specified by applying suitable boundary conditions to obtain the control-volume averaged values of the ghost cell.

During cavitation strong pressure pulses are generated. Non-reflecting boundary conditions are required that allow waves in the flow solution to leave the computational domain without any reflection at the in- and outflow boundaries. This is necessary to avoid that spurious reflected waves interfere with the time-dependent cavitating flow solution.

For the in- and outflow boundaries, the time-dependent, non-reflecting boundary conditions for the hyperbolic Euler equations with arbitrary equations of state, which are derived in Koop [12], are employed. These boundary conditions are based on the method of Thompson [19], who introduced an unified formalism for the time-dependent non-reflecting boundary conditions for the Euler equations using the perfect gas law as the equation of state.

The central concept is that a hyperbolic system of equations represents the propagation of waves and that at any boundary some of the waves are propagating into the computational domain while others are propagating outwards. The number and type of conditions at a boundary of a multi-dimensional domain are defined by the eigenvalues of the Jacobian of the component of the flux vector in the direction normal to the boundary. Each of the five eigenvalues λ_i represents the characteristic velocity at which a particular wave propagates. The behavior of outgoing waves is completely described by the solution within and at the boundary of the computational domain, while the behavior of the incoming waves is specified by data external to the computational domain.

Thus, because of the wave structure of the hyperbolic equations, the number of boundary conditions that may be imposed depends on the physics of the problem and may not be specified arbitrarily, i.e. the number of boundary conditions which must be specified at a point on the boundary is equal to the number of incoming waves at that point. The number of boundary conditions required at any point on the boundary may change in time. Also, the number of boundary conditions required at any time may vary with position on the boundary. For a subsonic inflow and a subsonic outflow four and one physical boundary conditions need to be specified, respectively.

For the solid walls on the hydrofoil and for the tunnel walls free slip boundary conditions are employed by using the non-permeability condition, i.e. $\vec{\mathbf{u}} \cdot \vec{\mathbf{n}} = 0$. The values in the ghost cells at the solid walls of the foil are obtained by applying the Curvature Corrected Symmetry Technique for unstructured grids as proposed by Wang and Sun [24].

GEOMETRY 3D TWIST HYDROFOIL

Foeth [4] has carried out experiments for a three-dimensional twisted hydrofoil placed in the cavitation tunnel of Delft University of Technology. The hydrofoil is denoted as Twist11 hydrofoil, because of its varying geometric angle of attack from $0°$ at the tunnel walls to $11°$ angle of attack at mid-section, see Dang [3], Koop *et al*. [11] and Foeth [4]. The chord length of the foil is equal to $c = 0.15$m. The foil spans the cavitation tunnel from wall to wall with the width of the tunnel equal to 0.3m, thus $s = 2c$. The foil is symmetric with respect to its mid-span plane.

The spanwise varying distribution of the local geometric angle of attack $\alpha(\bar{y})$ is designed to avoid interaction of the cavitation sheet with the tunnel wall. The local geometric angle of attack $\alpha(\bar{y})$ is defined by a cubic polynomial, such that it is α_{wall} at the tunnel wall, α_{max} at mid-span and that its derivative in spanwise direction is zero at the wall as well as at mid-span:

$$\alpha(\bar{y}) = \alpha_{\max}\left(2|\bar{y}|^3 - 3\bar{y}^2 + 1\right) + \alpha_{wall}, \quad (45)$$

where $\bar{y} = y / c$ is the dimensionless coordinate in span-wise direction $\bar{y} \in [-1,1]$, with $\bar{y} = 0$ defined to be at the mid-plane of the span and $\bar{y} = 1$ at the tunnel wall at the starboard side. Note that α_{wall} is the rotation angle of the entire hydrofoil, which is chosen to be equal to the local geometric angle of attack at the tunnel wall. The sections of the hydrofoil rotate around $\bar{x} = x / c = 0.75$ to reduce the optical blocking of the mid-section plane by the hydrofoil when viewing from the sides of the foil, which is illustrated in Figure 2(c), where the side view of the foil is presented. The foil considered is the Twist11 at $-2°$ geometric angle of attack, yielding $\alpha_{max} = 11°$ and $\alpha_{wall} = -2°$ in equation (45). The hydrofoil has a NACA0009 section with its half-thickness distribution given by

$$z = \frac{t}{0.2}\left(a_0\sqrt{\bar{x}} + a_1\bar{x} + a_2\bar{x}^2 + a_3\bar{x}^3 + a_4\bar{x}^4\right), \quad (46)$$

with $\bar{x} = x / c$, where the coefficients are equal to $a_0 = 0.2969$, $a_1 = -0.126$, $a_2 = -0.3516$, $a_3 = 0.2843$, $a_4 = -0.1015$ and with the thickness parameter $t = 0.09$. The hydrofoil is presented in Figure 2, where a 3D view, top view, side view and front view are shown.

Note that the distribution of the hydrodynamic angle of attack will be different from that of the geometric angle of attack. Due to the spanwise lift distribution there is a downwash on the central part of the hydrofoil and an upwash near the tunnel walls. This follows from Prandtl`s lifting line theory applied to the twisted foil, see [11].
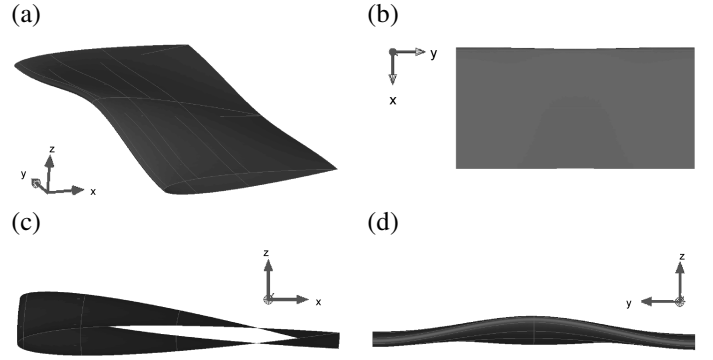

Figure 2: *3D Twist11 hydrofoil at α= -2˚, flow is in x-direction. (a) 3D view (b) top view (c) side view (d) front view.*

COMPUTATIONAL DOMAIN AND MESH

For numerical purposes the length of the test section is increased to minimize the effects of the implementation of the inlet and outlet boundary conditions. The hydrofoil is located in a channel with height $2c$, a length of $3c$ upstream of the leading edge, a length of $2c$ downstream of the trailing edge and a width of $s = 2c$. Note that for the numerical flow simulation only the starboard half of the test section and the foil is considered, because of its geometric symmetry and the assumed hydrodynamic symmetry.

The computational domain is divided into tetrahedral elements utilizing the software package ICEM-CFD. The surface of the foil is divided in 7 sub-surfaces, i.e. one surface wrapping around the leading edge and three surfaces on either side of the foil. Each surface has its own size of surface elements to ensure a fine mesh around the nose of the foil and a somewhat coarser mesh on the other surfaces of the hydrofoil. Note that the tetrahedrons close to the foil are much smaller than the tetrahedrons further away in the flow field.

Following a limited grid sensitivity study [11] it was concluded that for single-phase water flow a total number of around 350k tetrahedrons is adequate for a sufficiently accurate solution on the surface of the foil, which results in approximately 69k control volumes in the complete computational domain. For cavitating flow a tetrahedral grid with a refinement along the suction side of the hydrofoil is considered resulting in 205k control volumes. Both meshes are presented in Figure 3.

FULLY WETTED FLOW RESULTS

First, the numerical method is validated utilizing the experimental data of Foeth [4] for single-phase water flow. The angle of attack of the hydrofoil is $-2°$. The free-stream velocity U_∞, temperature T_∞ and pressure p_∞ are equal to $U_\infty = 6.75$ ms^{-1}, $T_\infty = 297$ K, $p_\infty = 0.97 \cdot 10^5$ Pa, respectively. At these conditions the pressures on the surface of the foil and the lift force on the foil have been measured. Foeth [4] reports a lift force of 455N, which amounts to a lift coefficient of $C_L = 0.46$.

The calculations are carried out with the first-order spatial reconstruction method for the first 50k iteration steps, after which the calculation is continued with the MUSCL type second-order reconstruction method applying the limiter method of Venkatakrishnan on the primitive variables *[ρ, u, v,*

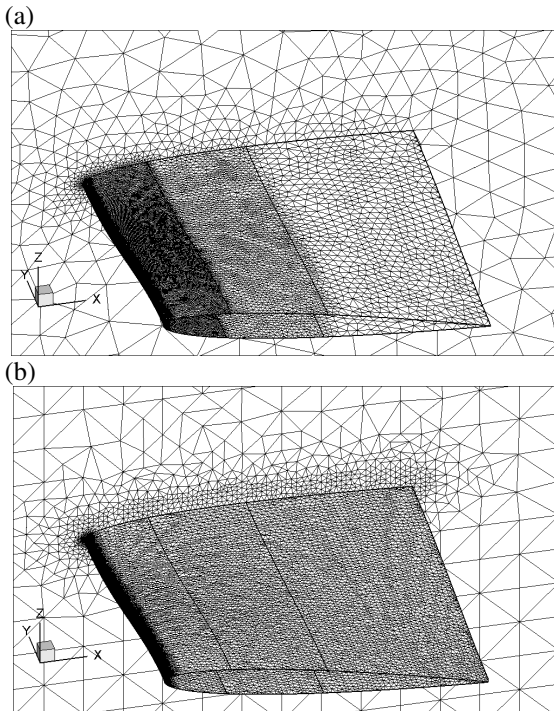$w, e]^T$. The calculations have been carried out on the coarse and fine mesh presented in Figure 3.

Figure 3: *Computational mesh for 3D Twist11 hydrofoil. α= -2˚ Flow is from left to right. (a) 357k tetrahedrons, 69k control volumes (b) 1,096k tetrahedrons, 205k control volumes*

It is found that during the calculation phase with the first-order reconstruction the computation converged rapidly. When switching to second-order the residuals decreased by two to three orders only. The reason for this stalling convergence behavior has been identified, see [12], to correspond to the very low Mach number in combination with the used limiter method for the second-order spatial reconstruction on unstructured grids. To improve the convergence behavior an additional calculation with the free-stream velocity increased from 6.75 ms^{-1} to $U_\infty = 50$ ms^{-1} has been carried out. For this higher velocity also a stagnating convergence is obtained, but at a two orders lower level.

In Table 3 the measured value for the lift coefficient is compared with the calculated values for the free-stream velocity $U_\infty = 6.75$ ms^{-1} on both grids and for $U_\infty = 50$ ms^{-1} on the coarse grid. The lift coefficient for $U_\infty = 6.75$ ms^{-1} is calculated to be equal to 0.445. Note that this value differs about 3% from the measured value of 0.46. It can be stated that this value is sufficient[1] accurately predicted by the present numerical method. The calculated lift coefficient on the coarse and fine mesh are approximately equal, which verifies that the coarse grid is adequate for a sufficiently accurate solution for single phase flow. For inviscid flow at low Mach number the

---

[1] *Foeth [4] mentions that his calibration was verified by placing weights on the hydrofoil in an empty cavitation tunnel. A deviation of 3% from the calibrated value was found and Foeth applied a correction in the lift coefficient for this discrepancy, which is in the same range as the difference between measured and predicted lift coefficient.*

lift coefficient for the velocities $U_\infty = 6.75$ ms^{-1} and $U_\infty = 50$ ms^{-1} should be about equal to each other, which is verified in Table 3.

For this case of three-dimensional inviscid flow the drag force will not be zero. The wake downstream of the trailing edge contains vorticity stemming from the difference in direction at the trailing edge of the velocity on the suction side and that on the pressure side resulting in a trailing vortex sheet. This trailing vorticity induces an upwash/downwash distribution at the foil which increases/decreases the local angle of attack experienced by the foil. This results in the so-called induced drag, see also [11] and [12].

From the good agreement between the experimentally obtained lift force and the calculated value and the agreement between the calculated lift coefficients for both velocities, we conclude that the present numerical method is capable of accurately predicting the lift force for low speed three-dimensional single-phase water flow.

Table 3: *3D Twist11 hydrofoil at -2˚ angle of attack. Measured lift coefficient and calculated lift and drag coefficients C_L and C_D for velocities $U_\infty = 6.75$ ms^{-1} on coarse and fine grid and $U_\infty = 50$ ms^{-1} on coarse grid. $p_\infty = 0.97 \cdot 10^5$ Pa, $\rho_\infty = 998.3$ kgm^{-3}, $T_\infty = 297$ K.*

U_∞ [ms^{-1}]	mesh	Numerical		Experimental
		C_D [-]	C_L [-]	C_L [-]
6.75	coarse	0.010	0.442	0.46
6.75	fine	0.0083	0.445	0.46
50	coarse	0.0098	0.454	-

In Figure 4 Foeth's measured C_p values at the surface of the hydrofoil are compared with the numerical results for the span positions, 50% (center), 40%, 30% and 20%, respectively. The experimental values are denoted by the open squares and the calculated values are presented with the closed circles.

As can be seen in Figure 4 the numerical results correspond reasonably well with the experimental data. However, the experimental value at $x/c = 0.3$ at 40% span appears to deviate from the numerical results. Foeth [4] mentions that the value from this sensor may not be reliable. Furthermore, an overshoot in $-C_p$ value at the trailing edge is observed in the numerical results. This is caused by the relatively badly shaped control volume around the trailing edge typical for a node-centered dual mesh. A solution has been found, see Hospers [7], by splitting the control volumes around the trailing edge in an upper and lower control volume allowing a discontinuous solution at the trailing edge.

In Figure 5 the distribution of $-C_p$ coefficient on the surface of the hydrofoil is presented for fully wetted water flow with $U_\infty = 50$ ms^{-1}. In the leading edge region on the suction side of the hydrofoil a clear low pressure region is visible. The design of the foil has been such that cavitation will occur in the center of the foil and that cavitation is avoided near the tunnel walls. Due to the span-wise varying angle of attack the pressure near the walls of the cavitation tunnel is much higher resulting in a lower $-C_p$ value.
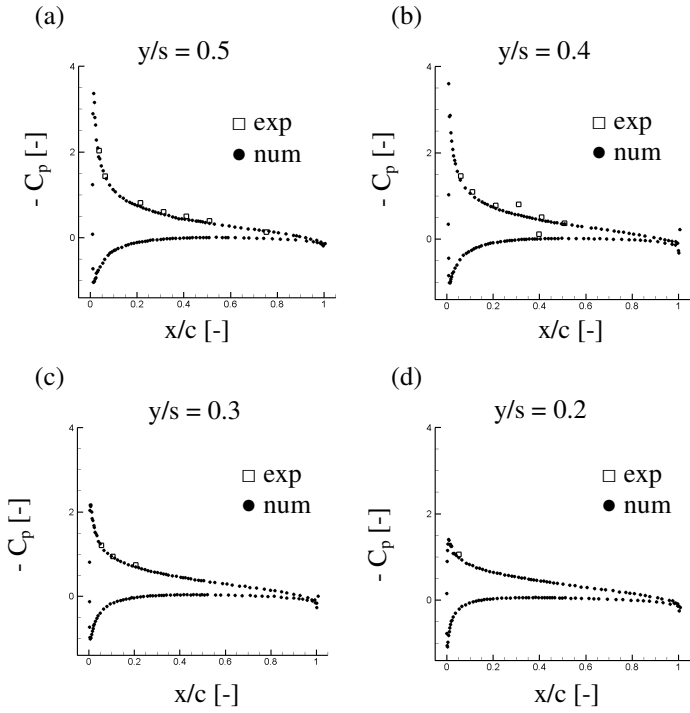
Figure 4: *3D Twist11 hydrofoil at α -2˚. Experimental (open squares) and numerical (solid circles) distribution of the -C_p coefficient for U_∞ = 50 ms^{-1}, T_∞ =297K, p_∞ = 0.97· 10^5 Pa, ρ_∞ = 998.2 kgm^{-3} (a) y/s = 0.5, (b) y/s = 0.4, (c) y/s = 0.3, (d) y/s = 0.2.*
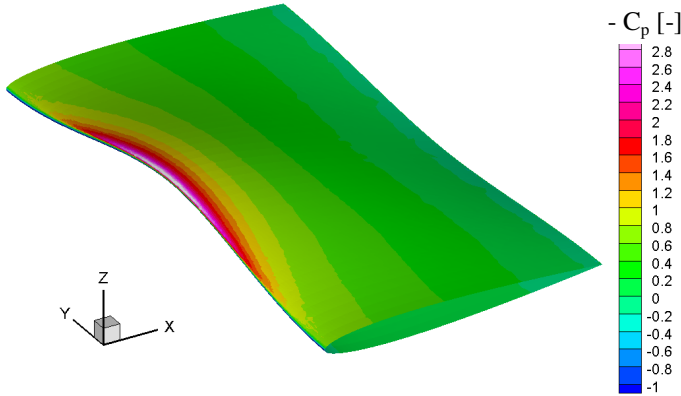

Figure 5: *3D Twist11 hydrofoil at α= -2˚. Distribution of -C_p coefficient on the surface of the hydrofoil. U_∞ = 50ms^{-1}, T_∞ = 297K, p_∞ = 0.97· 10^5 Pa, ρ_∞ = 998.2 kgm^{-3}.*

CAVITATING FLOW RESULTS

The unsteady cavitating flow about the 3D Twist 11 hydrofoil at -2˚ angle of attack is calculated and compared with the results of the experiments of Foeth [4]. Here the situation with steady inflow is considered at the cavitation number σ=1.1. The geometry is symmetric with respect to the mid-span plane and in order to save computational time only the starboard-half of the test section and hydrofoil is calculated. This assumption of hydrodynamic symmetry is supported by the experimental findings of Foeth. To speed up the formation and shedding of the cavity sheet in the numerical simulations, the calculations are performed at a free-stream velocity of U_∞ =

50 ms^{-1}. Note that to obtain a cavitation number equal to σ = 1.1 at a temperature of T_∞ = 297K a free-stream pressure equal to p_∞ = 13.75·10^5 Pa is chosen. To accelerate the calculations the numerical method has been parallelized by decomposing the computational mesh in 16 equal-sized blocks.

First, a solution employing the first-order reconstruction method is calculated on the coarse mesh. The sheet cavity is found to become steady for this mesh and order of reconstruction. The calculation is continued with the second-order reconstruction method on the coarse mesh. Then, it is found that resolution of the cavity sheet and its shedding is not represented adequately. The coarse mesh is too coarse to resolve the re-entrant jet and the shed vapor structures properly. The re-entrant flow is captured within one computational control volume and the sheet cavity occasionally sheds vortical vapor regions, which quickly dissipate.

To improve the resolution in the region with cavitation, the finer mesh as presented in Figure 3(b) is constructed by refining the region along the suction side of the hydrofoil to approximately 10% chord length in normal direction to ensure that the sheet cavity is located in this refined region. The solution obtained on the coarse grid is used as the initial solution for the calculations on the fine grid by employing a solution-interpolation method.

On the fine grid the corresponding numerical time step Δt_{cfl} is equal to Δt_{cfl} = 1.01·10^{-8} s. This small time step is required to meet the CFL condition and to be able to capture the pressure waves generated by the collapse of vapor structures. These waves travel at a velocity exceeding 1500 ms^{-1}.

The transient evolution of the cavitating flow can be illustrated through the time history of the total vapor volume V_{vap} as defined in Equation (7). This dimensionless quantity as a function of dimensionless time tU_∞/c is presented in Figure 6.
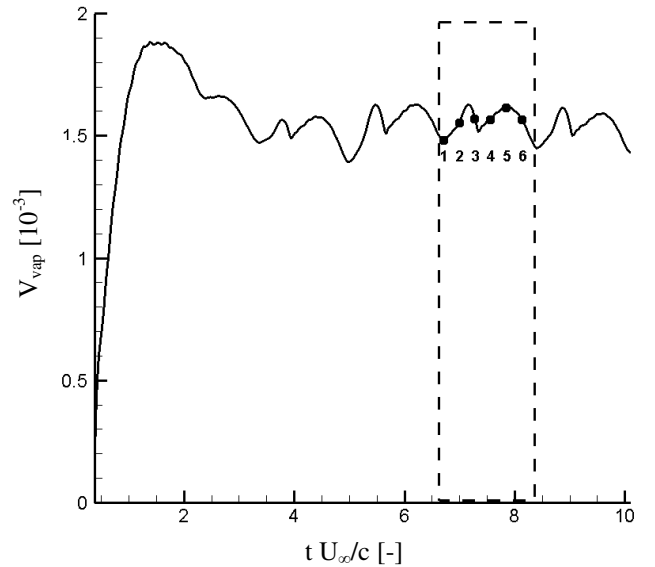

Figure 6: *Dimensionless total vapor volume V_{vap}, Equation (7), for cavitating flow about 3D Twist11 hydrofoil at α=-2˚, σ = 1.1. Fine grid, Δt_{cfl}=1.01·10^{-8}s.*

Figure 6 clearly indicates that after a start-up time, the evolution of the total vapor volume becomes periodic in time and that the amplitude and period of the cycle is constant in time. The cycle illustrated by the dashed box in Figure 6 has a dimensionless period of $TU_\infty/c = 1.7$, which corresponds to a Strouhal number based on the chord length equal to $St_c = 0.59$.

In Figure 7 the cavitation flow structures on the Twist11 hydrofoil are presented at the time instants 1-6 indicated in Figure 6. The time ΔT between each picture is equal to $8.5 \cdot 10^{-4}$ s or $\Delta T\, U_\infty/c = 0.28$. Two iso-contours of the void fraction are chosen to visualize the structure of the cavity sheet as can be seen most clearly in Figure 7(6).
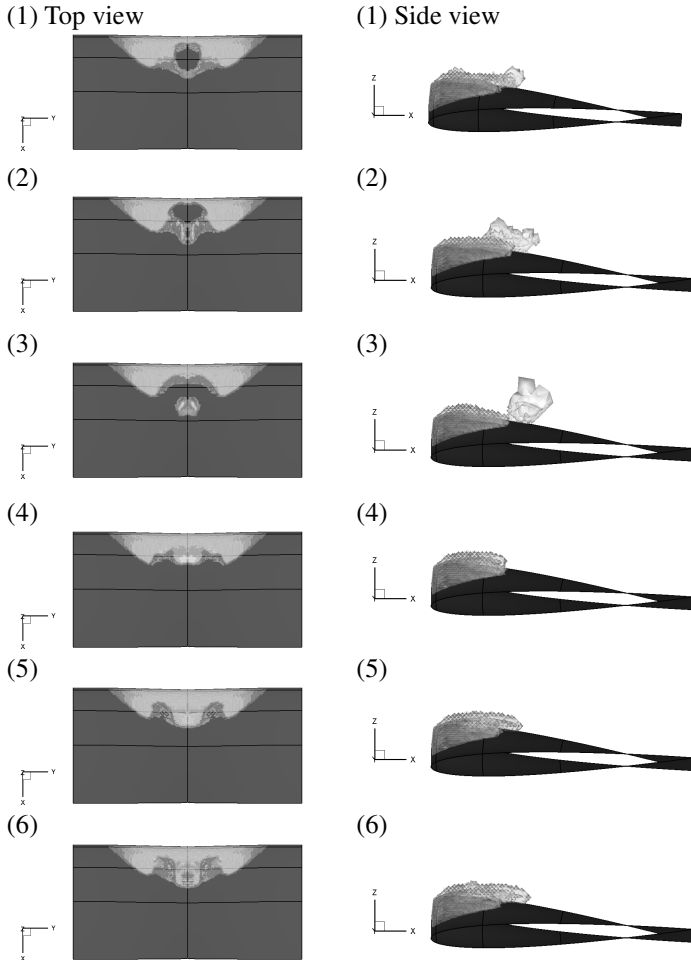
(1) Top view   (1) Side view

(2)

(3)

(4)

(5)

(6)

Figure 7: *Twist11 hydrofoil at α=-2˚ for σ=1.1. Formation of cavitating flow structures during one shedding cycle. Presented are the iso-contours of void fraction equal to α=10⁻³ and α=0.5. Pictures (1)-(6) correspond with points 1 - 6 in the time history given in Figure 6.*

In Figure 7(1) the total vapor volume is at its minimum. In the center of the hydrofoil the sheet cavity has disappeared and only a small spanwise cavitating vortex is visible. Also visible are two side lobes of the sheet cavity at one quarter and three quarters of the hydrofoil in span-wise direction. From Picture (1) to just after Picture (2) the total vapor volume increases, mainly due to an increase in volume of the detached vapor regions in the center of the hydrofoil. This detached vapor

region, shaped as a horseshoe, decreases in volume between Picture (2) and (3) until it has disappeared just after Picture (3). Meanwhile, the sheet cavity starts to grow again from the leading edge in the center of the hydrofoil from Picture (2) to Picture (6), which explains the increase of total vapor volume up to Picture (5). This increase is counteracted due to the formation of a re-entrant flow between Picture (4) and (5) starting at the closure region of the cavity sheet and extending towards the leading edge of the hydrofoil in Picture (6) after which the cycle is repeated continuously.

In his thesis Foeth [4] visualized and explained the structure of the shedding of the sheet cavity in detail and especially the formation of a cavitating horse-shoe vortex, the shape of the sheet cavity with distinct side-lobes and the formation of re- and side-entrant jets. In the numerical simulation the side-lobs of the sheet are clearly visible in Figure 7(3) just before the collapse of the cavitating horse shoe vortex. It should be noted that the conditions in the experiments are slightly different, i.e. α = -1˚ and σ = 1.13. However, the effect of the slight increase in angle of attack is counteracted by the slight increase in cavitation number and thus, the two conditions are expected to be very similar. Foeth [4] mentions that the overall shedding of the sheet cavity did not change much compared to the conditions of the numerical simulations, i.e. α = -2˚ and σ = 1.1.

A very distinct feature of the shedding of the sheet cavity on the 3D Twist11 hydrofoil is the formation of a cavitating horse-shoe vortex in the center part of the hydrofoil. In Figure 7(6)-(3) the formation and convection of such a cavitating horse-shoe vortex is clearly present in the numerical simulation. In Figure 7(6) the sheet cavity has reached its maximum extent in the center of the hydrofoil. Already a re-entrant flow is moving upstream along the surface of the hydrofoil generating a circulation at the closure region of the cavity sheet. As soon as the re-entrant flow reaches the leading edge, a spanwise cavitating vortex is detached from the sheet cavity as visible in Figure 7(1). This cavitating vortex is convected with the flow as visible in Figure 7(2) and (3). The center of the vortex is convected upward, primarily by its self-induced velocity, giving the vortex its horse-shoe shape. The height of the horse-shoe vortex is clear from the side view in Figure 7(3). It reaches up to 2-3 times the thickness of the sheet cavity. In the experiments of Foeth [4] the height of the shed vapor cloud is found to be an important feature.

In Figure 8 the streamlines on the surface of the hydrofoil are presented at the time-instants 1-6 of Figure 6. The streamlines are colored by the void fraction to indicate whether it is a liquid flow or a flow of vapor. The vectors indicate the direction of the flow.

In Figure 7(1) the vapor sheet in the center of the foil is at the leading edge of the foil and starts to grow. At the same time a flow of liquid is moving upstream, denoted by the blue color presented in Figure 8(1), and has reached the leading edge of the foil. Note the sharp transition from liquid to vapor at the mid-span of the hydrofoil in Figure 8(1).

There, the flow moves upward and impinges on the interface of the cavity sheet above the re-entrant flow. The fluid impinging on the interface cuts off a region of vapor as visible in Figure 7(1). Around this vapor region a circulatory flow
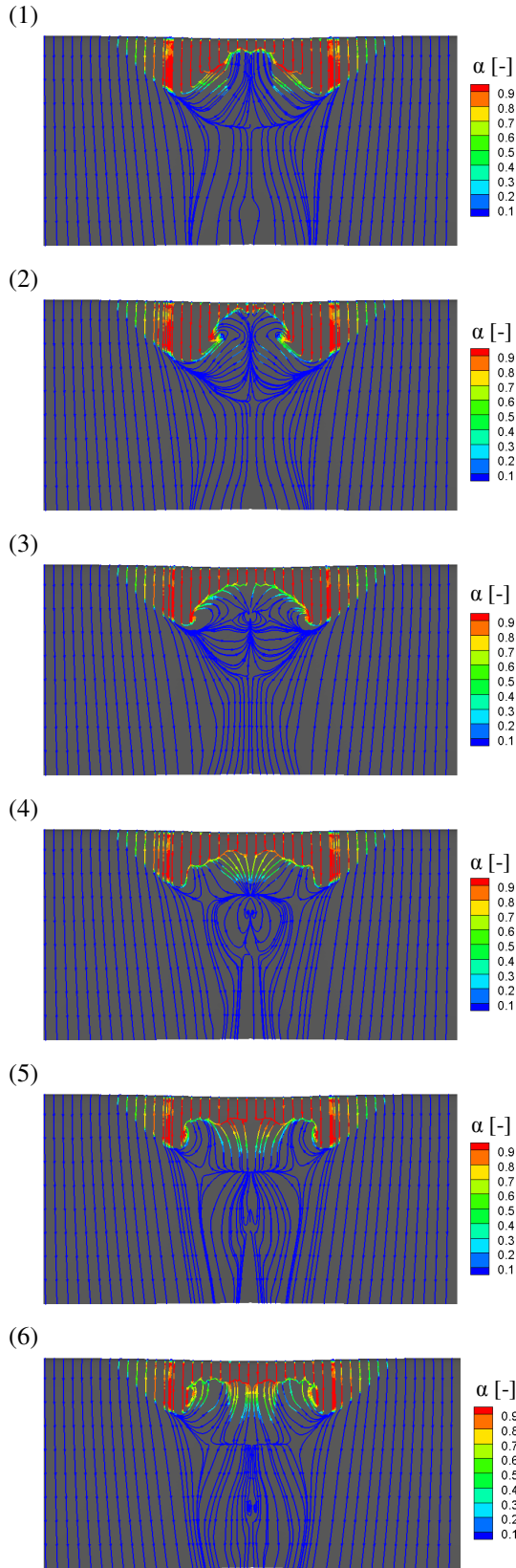
(1)

(2)

(3)

(4)

(5)

(6)

Figure 8: *Streamlines on surface of 3D Twist11 hydrofoil at α = -2˚, σ=1.1. Streamlines are colored by value of void fraction. Pictures (1)-(6) correspond with time-instants 1-6 presented in Figure 6.*

pattern is observed creating a spanwise (cavitating) vortex at the center of the hydrofoil, which is then convected with the flow as presented in Figure 8(2)-(5).

The shed cavitating vortex has disappeared between Pictures (3) and (4) and the sheet cavity grows to its longest extent at the center of the hydrofoil, see Figure 7(3)-(6). At the closure line of the sheet cavity a region with high vorticity has developed, which will drive the re-entrant flow. As visible in Figure 8(4) the re-entrant flow at the closure line of the cavity starts as a side-entrant jet. Note that during the growth of the sheet, a re-entrant flow is already moving upstream underneath the vapor sheet, see Figure 8(3)-(6), which is confirmed by the experimental results of Foeth [4]. In the present numerical simulations it appears that although an upstream moving liquid flow is already present just behind the cavity sheet, it does not have enough momentum to reach the leading edge until the vapor cloud has collapsed just after time-instant 3, see Figure 7(3) and Figure 8(3). More research, both experimentally as numerically, should be carried out to verify this observation. Also, the influence of the pressure pulses originating from the collapse of the vapor structures on the shedding mechanism and the formation of the re-entrant jet should be considered further.

We remark that in Figure 8(2) the re-entrant flow appears to be directed outward from the plane of symmetry resulting in a flow pattern on the surface of the hydrofoil which is in very close agreement with that of the experiments of Foeth [4].

Between Pictures (3) and (4) the shed vapor regions collapse near the surface of the hydrofoil creating strong pressure pulses that propagate over the surface of the hydrofoil. Three time-instants, t_1-t_3, are selected between Pictures (3) and (4). Denote the time at Picture (3) with t_0, then t_1 to t_3 are equal to $t_1 = t_0+1.8·10^{-4}$ s, $t_2 = t_1+10^{-5}$ s, and $t_3 = t_2+10^{-5}$ s, respectively. In Figure 9(I)-(III) the solution for the pressure and two iso-contours of the void fraction are presented for the times t_1-t_3, illustrating the origin and propagation of the pressure pulses above and on the surface of the hydrofoil.

In Figure 9(I) the convected vapor region reaches a region with higher pressure. Inside the vapor region the pressure is equal to the saturation pressure. This pressure difference induces a local flow field directed towards the center of the vapor region and causes the vapor region to collapse. The inward moving liquid impacts at the center of the former vapor region and initiates an outward propagating spherical shock wave traveling at the speed of sound c in the medium as presented in Figure 9(II). The maximum pressure in Figure 9(II) is 103 bar, which is 7.5 times the free-stream pressure $p_∞$.

In Figure 9(III) the shock wave is travelling radially outward from the region of collapse. Downstream the shock wave runs over the surface of the hydrofoil inducing a high loading on the foil. Upstream the shock wave hits the vapor sheet and due to the lower acoustic impedance $ρc$ of the two-phase flow region compared to that of the liquid, the shock wave is reflected as an expansion wave from the interface of the cavity sheet at which the pressure is constant. For the same reason the shock wave also reflects from the remaining vapor structures above the region of collapse.

As visible in Figure 9(III) the pressure again returns close to the saturation pressure at the location of the former vapor

region, which causes the liquid to cavitate again. In the present three-dimensional calculations the resolution of the computational mesh is not fine enough to capture this behavior in more detail. However, in Koop [12] we have shown that for two-dimensional cases this phenomenon is the reason for the so-called rebound of vapor clouds, which occasionally is observed during experiments.
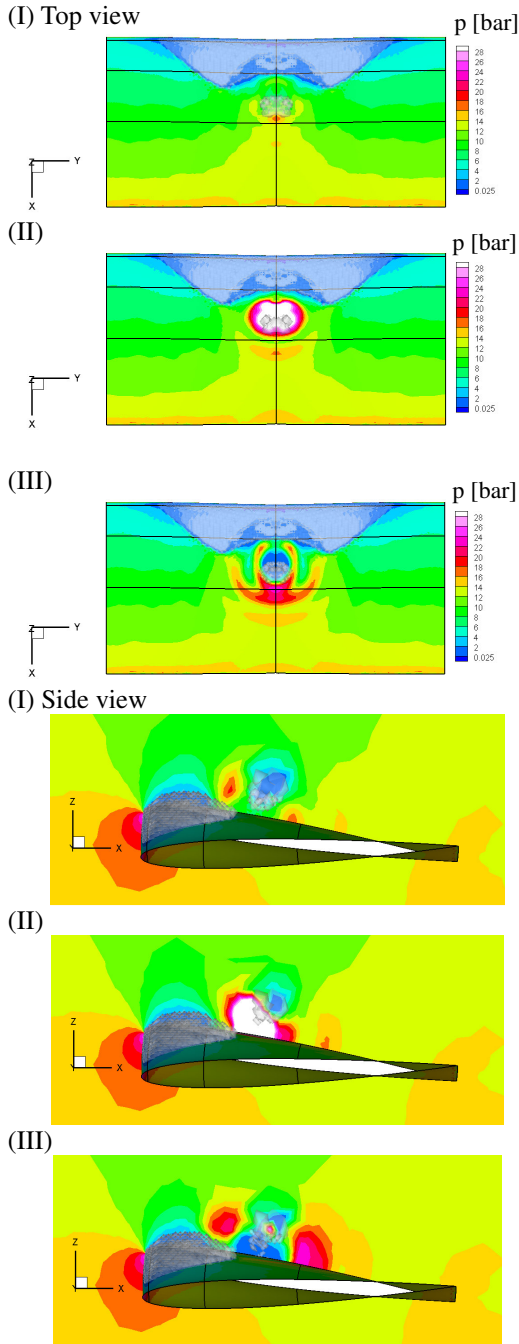
(I) Top view

(II)

(III)

(I) Side view

(II)

(III)

Figure 9: *Top and side view of collapse of shed vapor structures on 3D Twist11 hydrofoil at α= -2˚. Presented are two iso-contours of void fraction, i.e. α=10^{-3} and α=0.5 and solution for pressure p. Denoting time-instant 3 in Figure 6 with time t_0, then Pictures (I)-(III) correspond with times t_1 to t_3, where $t_1 = t_0 + 1.8 \cdot 10^{-4}$ s, $t_2 = t_1 + 10^{-5}$ s, and $t_3 = t_2 + 10^{-5}$ s, respectively.*

From Figure 9 we conclude that with the present mathematical and numerical formulation it is possible to capture pressure pulses in the liquid flow, which are generated by the collapse of vapor structures. These pressure pulses are believed to be the origin of erosion of surface material due to cavitation. Further calculations on a finer mesh should be carried out to focus more on the collapse phase of the shed vapor structures.

Note that between Figure 9(II) and (III) 1000 numerical time steps have been taken. It might be worthwhile to investigate methods such as multi-grid, preconditioning and/or implicit time-integration, which allow larger numerical time steps to be taken. However, the larger admissible numerical time steps should still resolve the propagion of high-frequency pressure pulses, which we believe to have a major influence on the self-oscillatory behavior of the sheet cavity and its shedding.

CONCLUSIONS AND DISCUSSION

In this paper the numerical results for the cavitating flow about the 3D Twist11 hydrofoil at -2˚ angle of attack are presented employing an equilibrium cavitation model in combination with the Euler equations. The used mathematical model for a compressible homogeneous water-vapor mixture at equilibrium saturation conditions offers a general applicable model for cavitation and does not have any free empirical parameters for phase transition.

First, it is shown that the numerical method is able to accurately calculate single phase water flow about the three-dimensional Twist11 hydrofoil compared to the experimentally obtained surface pressure data.

For cavitating flow we have found that the shape of the sheet cavity and the outline of the closure region as predicted by the present numerical method compare quite well with the experimental results of Foeth [4].

The 3D Twist11 hydrofoil has been designed to have a clear and controllable three-dimensional sheet cavity. It has been shown both experimentally by Foeth as numerically in this paper that the shape of the cavity and the closure line of the cavity determine the direction of the re-entrant flow and that the re-entrant flow from the sides dictates the behavior of the shedding cycle. Therefore, the shedding of a sheet cavity is governed by the direction and momentum of the re-entrant and side-entrant jets and their impingement on the cavity surface. The impingement of the re-entrant flow on the cavity interface and the detachment of a span-wise cavitating vortex is captured in the present numerical simulations based on the Euler equations. This confirms that these phenomena appear to be inertial in nature.

The development of a re-entrant flow is predicted in close agreement with that seen in the experiments. During the growth of the sheet, a re-entrant jet is already moving upstream underneath the vapor sheet. Note that the predicted re-entrant flow is a flow of liquid.

The formation of a cavitating horse-shoe vortex and its advection with the flow is captured in the present numerical simulations and these cavitating flow features agree quite well with the experimental observations.

We have shown that the present numerical method is capable to predict the collapse of shed vapor structures and the subsequent high pressure pulses on the surface of the hydrofoil, which is important for the prediction of erosion and noise. Within experiments it is a difficult task to capture and/or visualize these pressure pulses and the associated unsteady loading of the foils. In order to further validate the numerical method it is important to gain more knowledge experimentally and numerically on the strength of the pulses in combination with unsteady sheet cavitation. Furthermore, the influence of the pressure pulses on the shedding mechanism should be investigated both numerically as experimentally, especially the influence on the formation of the re-entrant jet.

At present the grid resolution is insufficient to be able to capture the phenomena related to smaller scale vapor structures. In the future methods need to be investigated to speed up the present numerical method. It might be worthwhile to investigate methods such as multi-grid, preconditioning and/or implicit time-integration, which allow larger numerical time steps to be taken. However, the larger admissible numerical time steps should still resolve the high-frequency pressure pulses, which we believe to have a major influence on the self-oscillatory behavior of the sheet cavity and its shedding.

The present paper focused on sheet cavitation on a stationary hydrofoil located in uniform inflow conditions. Foeth [4] also conducted experiments on hydrofoils placed behind two stacked hydrofoils with oscillating flaps generating an unsteady inflow. Huckriede [8] modeled these oscillating hydrofoils employing so-called 'transpiration' boundary conditions. The present research will be extended to numerically investigate the influence of unsteady inflow on the shedding of the cavitation sheet and compare the results with those of the experiments of Foeth.

In Koop [12] we also conducted numerical simulations for the steady cavitating flow about a finite three-dimensional wing generating a cavitating tip vortex. Future work has to be carried out to investigate the interaction between the sheet cavity and the cavitating vortex. One of the difficulties lies in accurately predicting the internal structure of the cavitating vortex. Ton [20], [21] has investigated the so-called 'Vorticity Confinement' method. There it is shown that it is indeed possible to improve the numerical results for tip vortices. However, it is also shown that the vorticity confinement method is not yet robust and needs to explored further.

ACKNOWLEDGMENTS

REFERENCES

[1] Batten, P, Clarke, N. Lambert, C. and Causon, D.M. *On the Choice of Wavespeeds for the HLLC Riemann Solver.* SIAM J. Sci. Comput. 18:1553-1570, 1997.

[2] Blazek, J., *Computational Fluid Dynamics: Principles and Applications,* Elsevier, 2nd edition, 2005.

[3] Dang, J. *Numerical Simulation of Unsteady Partial Cavity Flows.* PhD thesis, Delft University, 2001

[4] Foeth, E.J. *The structure of Three-Dimensional Sheet Cavitation,* PhD Thesis, Delft University of Technology, 2008.

[5] Guillard, H. and Viozat, C. *On the Behavior of Upwind Schemes in the Low Mach Number Limit.* Computers & Fluids, 28:63-86, 1999.

[6] Harten, A., Lax, P.D. and van Leer, B. *On Upstream Differencing and Godunov-type Schemes for Hyperbolic Conservation Laws*, Siam Review, 25:35-61,1983.

[7] Hospers, J.M. *Development and Application of Hybrid Grids for Finite Volume Methods*, Masters's thesis, University of Twente, 2007

[8] Huckriede, K.W. *Transpiration boundary condition for numerical study of unsteady 2D sheet cavitation on hydrofoils*, Master`s thesis, University of Twente, 2008

[9] The International Association for the Properties of Water and Steam; http:/www.iapws.org/.

[10] Jameson, A. Schmidt, W. and Turkel, E. *Numerical Solution of the Euler Equations by Finite Volume Methods Using Runge-Kutta Time-Stepping Schemes.* AIAA paper, 91-1259, 1981

[11] Koop, A.H., Hoeijmakers, H.W.M. Schnerr, G.H. and Foeth, E.J. *Design of Twisted Cavitating Hydrofoil using a Barotropic Flow Method*, CAV2006, Wageningen, 2006

[12] Koop, A.H. *Numerical Simulation of Unsteady Three-Dimensional Sheet Cavitation*, PhD Thesis, University of Twente, the Netherlands, 2008

[13] Leer, van B. *Towards the Ultimate Conservative Difference Scheme V. A Second-order Sequel to Godunov`s Method.* Journal of Computational Physics, 32:101-136, 1979

[14] Liou, M.S. *A Sequel to AUSM, Part II: AUSM+-up for all speeds.* Journal of Computational Physics, 214:137-170, 2006.

[15] Saurel, R. Cocchi, J.P. and Butler, J.B. *A Numerical study of Cavitation in the Wake of a Hypervelocity Underwater Profile.* Journal of Propulsion and power. 15(4):513-522, 1999

[16] Schmidt, S.J., Sezal, I.H., Schnerr, G.H. *Compressible Simulation of High-Speed Hydrodynamics with Phase Change.* ECCOMAS CFD, 2006

[17] Schmidt, E. *Properties of Water and Steam in SI-Units; 0-800˚C, 0-1000 bar.* Springer-Verlag. R. Oldenbourg, 4th, enlarged printing edition, 1989.

[18] Schnerr, G.H. Sezal, I.H. and Schmidt, S.J. *Numerical Investigation of Three-Dimensional Cloud Cavitation with Special Emphasis on Collapse Induced Shock Dynamics,* Physics of Fluids, 20:040703, 2008

[19] Thompson, K.W. *Time Dependent Boundary Conditions for Hyperbolic Systems II*, Journal of Computational Physics, 89:439-461, 1990

[20] Ton, T.A. *Vorticity confinement in Compressible Flow, Implementation and Validation*. Master`s thesis, University of Twente, 2008

[21] Ton, T.A., Koop, A.H., Hoeijmakers, H.W.M. and De Vries, H. *Investigation of Vorticity Confinement in Compressible Flow*, AIAA 092407, 2009

[22] Toro, E.F. Spruce, M. and Speares, W. *Restoration of the Contact Surface in the HLL-Riemann solver.* Shock Waves, 4:25-34, 1994.

[23] Venkatakrishnan, V. *Convergence to Steady-State Solutions of the Euler Equations on Unstructured Grids with Limiters*. Journal of Computational Physics, 118:120-130, 1995.

[24] Wang, Z.J. and Sun, Y. *Curvature-Based Wall Boundary Condition for the Euler Equations on Unstructured Grids.* AIAA Journal, 41:27-33, 2003

[25] Weiss, J.M. and Smith, W.A. *Preconditioning Applied to Variable and Constant Density Flows,* AIAA Journal, 33(11):2050-2057, 1995